The Space Congress® Proceedings

1968 (5th) The Challenge of the 1970's

Apr 1st, 8:00 AM

Fluidic Attitude Control System — Solar Probe

D. B. Wall
Martin Marietta

B. W. Patz
Martin Marietta

FLUIDIC ATTITUDE CONTROL SYSTEM

~ SOLAR PROBE ~

by
Dr. D. B. Wall and Dr. B. W. Patz

Martin Marietta Corporation
Orlando, Florida

Summary

This paper establishes design criteria for a fluidic attitude control system for a solar probe*. Results of an analytical and experimental investigation are presented to indicate that fluidic control is both possible and practical.

A system is designed to meet the control system requirements. A block diagram of the control system is discussed and derivations of the transfer functions explained. The system response is determined for the radii of 1 AU maximum and 0.3 AU minimum.

System performance is described and computer solutions for the vehicle's attitude response obtained. Performance is discussed in terms of two separate modes of operation: a short-term mode (hundreds of seconds) and a long-term mode (thousands of seconds). As a result of this system analysis, an important parameter, called the "normalized system gain," appears. This parameter is useful in scaling the spacecraft in order to design the short term response of the simulator.

Problems associated with simulator fabrication and performance are discussed and experimental data on its performance presented. Fabrication of the components, components characteristics, and component integration are also discussed.

Introduction

A Martin Marietta study of the objectives and design considerations of a solar probe was reported in 1963[1]. At that time, the fundamental features of a solar probe were defined. The present phase of the solar probe study was undertaken to establish design criteria for a fluidic attitude control system and to verify the feasibility of fluidic control through the design, construction, and use of a single-degree-of-freedom simulator.

The simulator exhibited the necessary stabilization in response to anticipated disturbances. Moreover, the model's response was not adversely affected by an earth environment as opposed to the "weightless" environment of free space.

The application of fluidic devices in solar probe spacecraft attitude control systems is particularly promising. Compared to contemporary electronic-electromechanical devices, they are potentially more reliable and intrinsically less susceptible to temperature and nuclear radiation environments. They are especially suited to missions in which the spacecraft is exposed to extreme environments. Because they have few hardware components, fluidic control systems are relatively simple to mechanize.

Solar Probe Mission

Data available on the sun and its atmosphere and the conflict of theory regarding the dynamic corona indicate the need for additional experimental data. Experiments should resolve the important unknowns in the structure of the solar magnetic field and the mechanisms of the corona. The spacecraft should approach as close as 0.3 AU (1 AU = 1 earth orbit radius) to the sun if the scientific objectives of a solar probe are to be reasonably satisfied[1].

The most practical compromise values of perihelion radius, corona sampling time, and spacecraft lifetime are 0.3 AU, 70 days, and 1 year. These figures serve as a basis for defining the lifetime, vehicle inertias, solar radiation, and heat environment for which the control system will be designed[2].

The flight plan for the solar probe mission is depicted in Figure 1. This illustration shows the probe's position at various times in relation to the sun and earth.

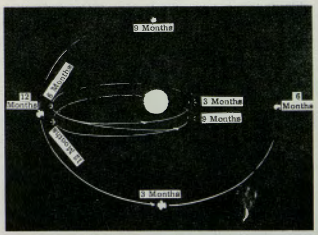

Fig 1. Solar Probe Flight Plan

Vehicle Control System

Requirements

The primary functions of the attitude stabilization and control system during the coast phase of the solar probe mission are to maintain the orientation of the heat shield and solar panels to the

*Contract NAS 12-127 from NASA Electronics Research Center.

sun line during the entire flight, and provide a complete three-axis attitude reference for use in analyzing the experimental data and orienting the high-gain communication antenna. The attitude control system performance requirements[1] are summarized in Table I and the significant disturbance sources in Table II.

TABLE I

Pitch or Yaw Errors

Allowed Error or Error Rate	Requirement Reason
±1 deg	Antenna alignment
±5 deg	Vehicle and solar panel alignment

TABLE II

Significant Disturbance Source in Yaw or Pitch

Disturbance	Cause
0.0846 deg/s (V_o) 0.01 probability	Meteor impact
9,000 x 10^{-8} ft lbf (1,200 x 10^{-7} N-m)	Maximum expected solar torque due to unknown center of pressure
2,400 x 10^{-8} ft lbf (325 x 10^{-7} N-m)	Average expected solar torque

The largest disturbance is that caused by meteor impact. Previous studies[2] developed the meteor impact disturbance as a 0.01 probability for the entire mission. All other disturbances are insignificant compared to the 0.0846 degree-per-second perturbation caused by meteor impact.

Description

The solar probe's attitude stabilization and control in yaw and pitch are provided by the elements, and in the manner indicated below:

1. Sun sensors sense the attitude deviation in yaw and pitch;
2. Flywheels spin up to remove angular momentum from the solar probe;
3. Movable vanes make use of solar radiation pressure to remove angular momentum from flywheel and maintain attitude error about the null;
4. Design places the center of solar radiation pressure aft of the center of mass to yield a static stability margin.

Figure 2 is a schematic of the fundamental implementation for pitch and yaw stabilization and control. Roll stabilization and control are provided by another system. The essential differences between the roll system and the yaw and pitch system are provision of a star sensor instead of a sun sensor, and gas jets to despin the flywheel instead of solar vanes.

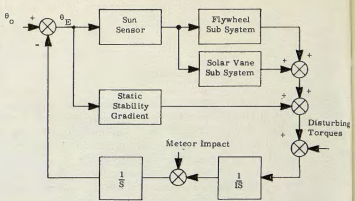

Fig 2. Attitude Stabilization and Control System

The primary components of the sun-sensor are an optical unit and a fluidic bolometer. The optical unit is a lens that focuses the sun's rays on the bolometer, while the bolometer is a balanced bridge network composed of two capillary tubes and two variable orifices. When the sun is focused on the capillary tubing, the heat conducted to the fluid passing through the tubing causes a viscosity change in the fluid. A pressure differential, therefore, is developed across the bolometer coils as a function of the vehicle's attitude. The bolometer output possesses small angle linearity; however, when an error greater than 4 degrees is imposed, the output exhibits a noticeable nonlinearity. The bolometer output also exhibits a first order lag due to thermal capacity associated with the bolometer.

The flywheel subsystem consists of fluidic amplifiers and a flywheel. The fluidic amplifiers deliver a differential mass flow rate proportional to the output differential pressure from the bolometer. The output of the last fluidic amplification stage impinges on the flywheel and, therefore, spins it up. The rate of change of the flywheel's angular momentum produces a torque on the solar probe that changes the probe's rate of spin. When the flywheel has spun up, the solar probe is no longer spinning.

The stabilizing vanes, consisting of a fluidic drive that extends the DeHavilland booms at a rate of not more than 0.078 ft/s (0.0234 m/s) and an extension of not more than 45 ft (13.7m) are decidedly nonlinear. Not only is there a change in torque due to solar radiation acting on the vanes, but also a change due to an increase in the moment of inertia of the vehicle as the booms are extended. A complete block diagram of the coast phase control system is shown in Figure 3.

Performance

The exact solution for the single-axis solar probe was determined by a computer simulation of the system represented by the block diagram

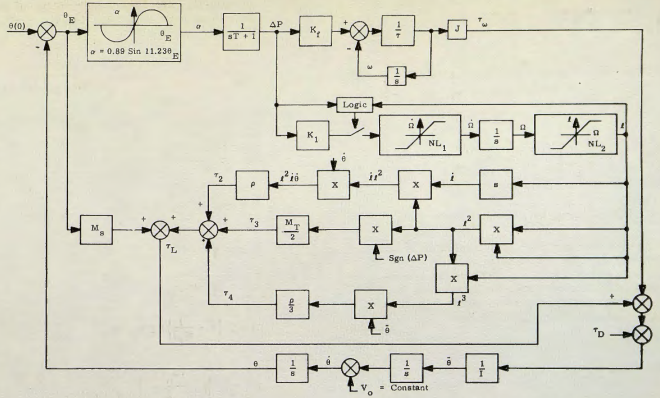

Fig 3. Complete Single-Axis System

shown in Figure 3. Because the simulation indicated that the control actually takes place in two modes, a two-mode approximation is developed. The performance of the system's short-term and long-term modes can be understood by investigating the relative magnitude of the apparent torques acting on the solar probe.

Figures 4 and 5 plot the extreme values of the underdamped flywheel torque and the actual value of solar vane torque at 1 AU and 0.3 AU distances from the sun. The torque due to the static stability gradient is always less than the lowest scale shown; hence, the static stability can be neglected in that it amounts to less than a 4 percent error for the long-term mode solution. Figures 4 and 5 reveal also that the short-term mode is dominated by the flywheel and that the solar vanes

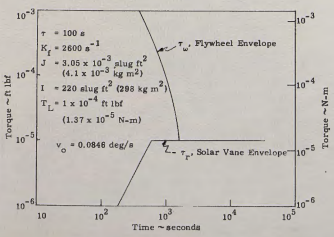

Fig 4. Flywheel and Solar Vane Torque vs Time at 1.0 AU

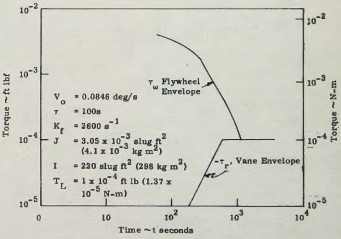

Fig 5. Flywheel and Solar Vane Torque vs Time at 0.30 AU

dominate the long-term mode. Physically, the flywheel is spun up (hundreds of seconds) to remove the vehicle's angular momentum. Eventually (thousands of seconds) torque from the solar vanes remove the flywheel's angular momentum.

The block diagram presented in Figure 6 can be used as an approximation of the system shown in Figure 3, for a maximum attitude error, θ_{max}, of less than 6 degrees. If θ_{max} is allowed to go beyond 6 degrees, the system design becomes more complicated and the bolometer nonlinearity must be included. This nonlinearity causes the actual system to be unstable at the low gains associated with large overshoots, whereas the linear model does not indicate this instability. The nonlinearity and time constant of the bolometer can

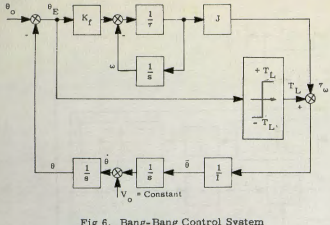

Fig 6. Bang-Bang Control System

be neglected because they cause less than a 7-percent error in the short-term solution when θ_{max} is less than 6 degrees. The vanes are approximated by a bang-bang system because the time for them to fully extend is small compared to the period of the long-term mode.

System Analysis

The system shown in Figure 6 is now treated analytically. The operational equation for $\dot{\theta}(S)$ in terms of the meteor impact parameter, V_o, and the torques acting on the system, is

$$\dot{\theta}(S) = V_o(S) + \frac{1}{IS}\left[\tau_\omega(S) + \tau_L(S)\right] \quad (1)$$

where

$$\tau_\omega(S) = -\frac{SK_fJ\,\theta(S)}{(S\tau + 1)}$$

and, for the time domain, with τ_L written as

$$\tau_L(t) = -\frac{T_L\,\theta}{|\dot{\theta}|} \quad . \quad (2)$$

Transforming Equation (1) and substituting Equation (2) therefore yields

$$\frac{d^2\theta}{dt^2} + \frac{1}{\tau}\frac{d\theta}{dt} + \frac{JK_f}{I\tau}\theta = \frac{V_o}{\tau} - \frac{T_L}{I}\frac{\theta}{|\dot{\theta}|} - \int_o^t \frac{T_L}{I\tau}\frac{\theta}{|\dot{\theta}|}\,dt. \quad (3)$$

The solution to Equation (3) can be obtained by changing the sign of T_L each time θ changes sign, first for $\theta \geq 0$, then reversing the sign on T_L and including $\dot{\theta}$ at $\theta = 0$ for the new solution. This procedure is repeated every time θ passes through zero. Before developing this solution, however, it should be noted that the coefficients of the differential equation are determined by three "similarity" parameters: $1/\tau$, JK_f/I, and T_L/I. Since these coefficients determine the time response of the system, any two solar probe control systems for which the assumptions used to derive the solutions are valid and have identical "similarity" values will have identical short- and long-term response characteristics. The solution for $\theta \geq 0$ is

$$\theta = D + Ct + e^{-t/2\tau}\left[E \sin \phi t - D \cos \phi t\right] \quad (4)$$

where

$$\omega_n = \sqrt{\frac{JK_f}{I\tau}}$$

$$\zeta = \frac{1}{2\tau\omega_n}$$

$$\phi = \omega_n\sqrt{1 - \zeta^2}$$

$$C = -T_L/JK_f$$

$$D = C\left\{\tau - \frac{I}{K_fJ}\right\} + I\,V_o/JK_f$$

$$E = \frac{V_o}{\phi}\left\{1 - \frac{(\omega_n\tau)^{-2}}{2}\right\} + \frac{T_L}{\phi JK_f}\left\{1.5 - \frac{(\omega_n\tau)^{-2}}{2}\right\} \quad (5)$$

This analysis is the basis for Figures 7 and 8. Figure 7 compares the maximum attitude error, θ_{max}, with the normalized system gain, JK_f/I, and the flywheel time constant, τ, for a meteor impact that produces the maximum attitude error rate of 0.0846 deg/s, and thus shows that JK_f/I must be larger than 0.0368 s^{-1} when τ = 100s to stay within the 5-degree maximum attitude error limitation. Figure 8 plots the time to reach the maximum attitude error versus the normalized gain constant and τ, e.g., if $T_L/I = 0.0368\ s^{-1}$ and τ = 100s, then t_p = 99s.

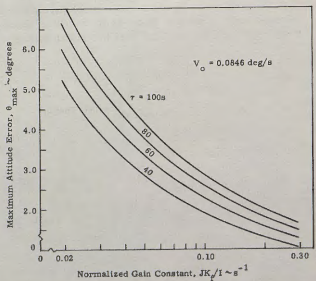

Fig 7. Maximum Attitude Error vs Normalized Gain Constant

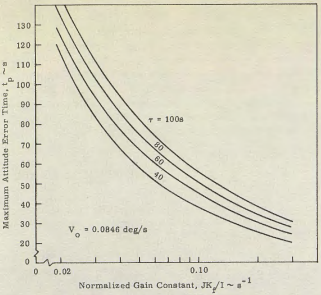

Fig 8. Time to Reach Maximum Attitude Error vs Normalized Gain Constant

Figure 9 compares the T_f (attitude error null time) and T_L/I (normalized maximum solar vane torque) for both the bang-bang model and the actual system obtained by simulation. For example, if $T_L/I = 1.25 \times 10^{-6}\ s^{-2}$, then $T_o = 10^3$s for the bang-bang system and 1.4×10^3s for the actual system as read from the lower curve and, if $T_L/I = 2.5 \times 10^{-8}\ s^{-2}$, then $T_o = 5.0 \times 10^4$s for both the bang-bang system and the actual system as read from the upper curve.

It is shown in Figures 7 and 8 that the solar probe can be scaled for the short-term mode where the scaling parameters are JK_f/I and τ.

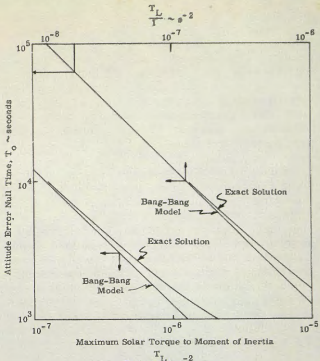

Fig 9. Attitude Null Time vs Ratio of Maximum Solar Vane Torque to Vehicle Moment of Inertia

Likewise, it is shown in Figure 9 that the long-term mode can also be scaled with the scaling parameter being T_L/I.

The system shown in Figure 3 was simulated on a digital computer. Figure 10 shows the results of two runs for attitude error versus time

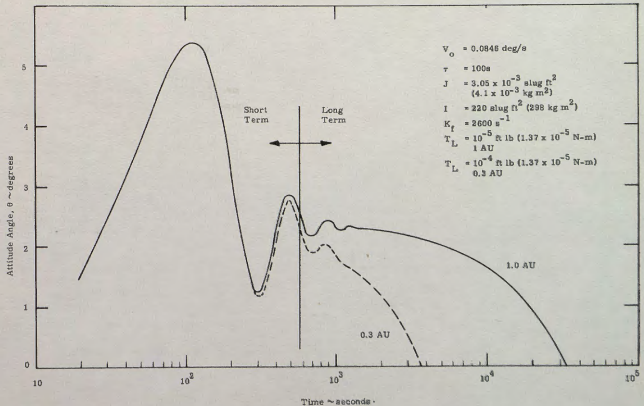

Fig 10. Time vs Attitude Angle for Long- and Short-Term Modes

for some representative values of the system parameters. The values for solar righting torque and static stability gradient were chosen to agree with the reference values. The values for the system variables were chosen by means of the two-mode approximation (the bang-bang model) for a maximum attitude error of 5 degrees. Figure 10 clearly shows the existence of independent short-term and long-term modes, with the long-term mode a function of solar radiation pressure (the distance from the sun).

Tables III and IV compare the θ_{max} and T_o values for both the actual system and the simplified bang-bang model. It can be seen that the approximate system yields a solution in θ_{max} with less than 7 percent error over the range of values covered in Table III, and to less than 13 percent error for T_o in Table IV. The 7 percent error in θ_{max} is mainly due to the bolometer nonlinearity, whereas the 12.4 percent error in T_o is due to the time required to extend the solar vanes. This last error is fixed at about 400 seconds, which is less than the 600 seconds to extend the vanes, due to averaging the solar radiation torque over the 600 seconds.

TABLE III

Comparison of θ_{max} Values Between Actual System Simulation and Two-mode Model Approximation

($JK_f/I = 0.0361\ s^{-1}$; $T_L = 1.36 \times 10^{-5}$ Newton-meters)

τ (s)	θ_{max} (deg)		Error (% of Actual)
	Model	Actual	
20	2.74	2.85	3.9
100	5.03	5.39	6.7

TABLE IV

Comparison of T_o Values Between Actual System Simulation and Model Approximation

($JK_f/I = 0.0361\ s^{-1}$; $\tau = 100s$)

T_L (N-m)	T_o (s)		Error (% of Actual)
	Model	Actual	
1.36×10^{-4}	3.19×10^3	3.65×10^3	12.4
1.36×10^{-5}	3.24×10^4	3.29×10^4	1.5

Developed below is the approximate nonlinear solution when the bolometer nonlinearity is included without the time constant. Solution of the nonlinear model is a much better approximation to the actual system's response if larger attitude errors are allowed; however, if θ_{max} is less than 6 degrees the linear model is adequate for model design and basic system understanding.

Figure 11 illustrates the complete block diagram of the simulator, including both the bolometer's time constant and its nonlinearity. The diagram has been arranged to facilitate computer mechanization of the equations. The following analysis assumes the time constant of the bolometer is negligible, but includes the bolometer nonlinearity (the short period solution may be obtained by neglecting the reaction jets):

$$\theta(S) = \frac{V_o(S)}{S} + \frac{K_f J}{I} \frac{1}{(S\tau + 1)} \frac{\theta_p}{S(S\tau + 1)} \qquad (6)$$

Since T is negligible and considering initial conditions, $(\theta, \dot{\theta}) = (0, V_o)$, Equation (6) may be transformed to yield $\theta(t)$

$$\frac{d^2\theta}{dt^2} + \frac{1}{\tau}\frac{d\theta}{dt} = \frac{V_o}{\tau} + \frac{K_f J}{I\tau}\theta_p(t) \qquad (7)$$

where

- T = bolometer time constant of 2s (neglected)
- τ = flywheel time constant of 100s
- K_f = composite gain of bolometer, fluidic amplifiers, and flywheel
- J = moment of inertia of flywheel 3.05×10^{-4} slug ft^2 (4.1×10^{-4} kg-m^2)
- I = moment of inertia of solar probe simulator 2 slug ft^2 (2.7 kg-m^2)
- τ_L = torque produced by reaction jet (N-m) (neglected)
- V_o = design initial velocity input due to meteor impact (0.0014763 rad/s)

with initial conditions on both θ and ΔP at zero.

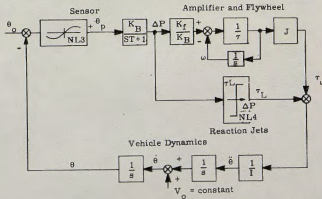

Fig 11. Simulator

It was demonstrated previously that τ_L may be dropped in the short period analysis since its contribution to $\theta(t)$ is negligible. θ_p has been experimentally determined to be

$$\theta_p = -0.089 \sin 11.23\,\theta \qquad (8)$$
$$\text{for } |11.23\theta| \leq \pi$$

and

$$\theta_p = 0, \text{ for } |11.23\theta| > \pi$$

Therefore, Equation (7) may be written

$$\frac{d^2\theta}{dt^2} + \frac{1}{\tau}\frac{d\theta}{dt} + \frac{(0.089)K_f J}{I\tau} \sin 11.23\theta = \frac{V_o}{\tau} \quad (9)$$

for $|11.23\theta| \leq \pi$. The parameters JK_f/I and τ are unique in specifying the system response. Thus, even when the bolometer nonlinearity is included, the short term response is specified for a given disturbance, V_o, by JK_f/I and τ.

Equation (9) may be recognized as in the same form as the equation for a damped pendulum or a phase demodulator. The equation is second order so that the phase plane can be used to describe completely the solutions. It has a stable focus at

$$\frac{(0.089)\,K_f J}{I\tau} \sin 11.23\theta = \frac{V_o}{\tau}, \text{ for } |11.23\theta| < \frac{\pi}{2}$$

and a saddle point at

$$\frac{(0.089)\,K_f J}{I\tau} \sin 11.23\theta = \frac{V_o}{\tau}, \text{ for } |11.23\theta| > \frac{\pi}{2}.$$

If no real singular point exists, then the system must always be unstable.

Figure 12 is a phase portrait of the solar probe simulator without reaction jets. It shows the separatrix separating all stable solutions from unstable solutions and a typical trajectory for a meteor impact. Solution of the nonlinear model leads to a determination of the values of $K_f J/I$ and τ which will result in a stable system. The system can become unstable when the bolometer nonlinearity is included if K_f decreases sufficiently or if τ increases sufficiently. Figure 13 is a plot of the stability boundary for this system. It is a plot of $K_f J/I$ versus τ for a meteor impact which causes $\dot{\theta}$ to be 0.0846 degree per second.

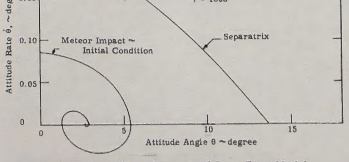

Fig 12. Phase Plane Portrait of Bang-Bang Model Without Reactions Jets

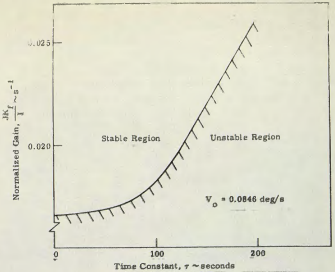

Fig 13. Normalized Gain vs Flywheel Time Constant

Simulator

Description

A simulator to demonstrate the coast phase attitude control system performance has been designed, built, and tested. This simulator has no solar vanes but employs reaction jets for the long-term restoration torque. Figure 10 and Tables I and II have demonstrated that the bang-bang model yields a solution that matches accurately the actual system. Figures 7, 8, and 9 show the system scaling. The normalized gain constant and the normalized maximum solar vane torque in these figures also provide the necessary scale factors. The solar probe simulator contains all the significant features of the actual system and has characteristics and properties that may be scaled conveniently for laboratory experimentation.

The simulator consists of an air bearing pad, a movable platform (containing the control system within the plastic box), and the sun substitute. A photograph of the simulator is given in Figure 14 and the parameters in Table V.

TABLE V

Simulator Parameters

Moment of Inertia (I)	2.0 slug ft^2 (2.71 kg m^2)
Moment of Inertia of Flywheel (J)	3.05×10^{-4} slug ft^2 (4.1×10^{-4} kg m^2)
Fluidic Gain (K_f)	1,400 s^{-1}

The input to the bolometer is the relative angle of the bolometer's center line compared to a radial sun line. When both lines are coincident, the bolometer output is nulled. The output of the bolometer is thus a differential pressure which is a function of the angle between the two lines.

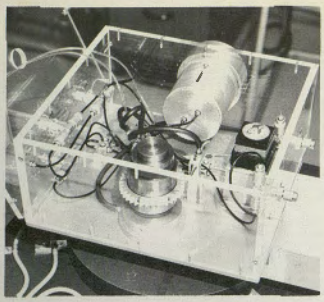

Fig 14. Reaction Flywheel and Simulator

The output of the bolometer is supplied to the analog amplifier package, and the output from the amplifier package is then supplied to the reaction wheel and the solar vane torque simulators (reaction jets).

The bolometer senses angular deviation from the spacecraft-sun line. The method used to accomplish this is to sense differentially the total solar radiation available by directing the solar flux to impinge unequally on a pair of coils (Figure 15). When more solar radiation falls on one coil than the other, a differential pressure is obtained. The curve in Figure 16 represents the bolometer output pressure versus the sun-line angle. The data indicate an average static pressure gain of 0.54 psi/rad (3.70 kN/m^2-rad) under loaded conditions, i.e., driving the first stage amplifier.

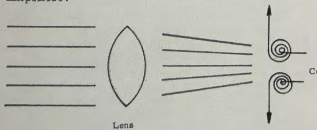

Fig 15. Bolometer

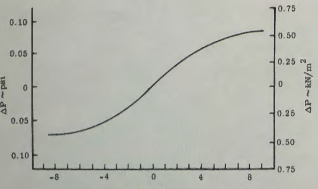

Fig 16. Bolometer Output vs Sun-Angle Offset

Tests performed on the bolometer determined an efficient operating quiescent pressure. After the power differential for full excursion had been evaluated, a quiescent of 2 psi (13.79 kN/m^2) was chosen. At this value, a power differential of 0.002 watts will be realized at the input to the amplifier. Figure 17 illustrates the amplifier package schematic.

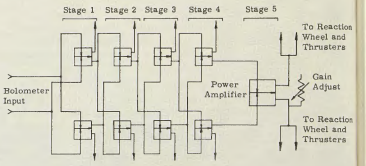

Fig 17. Amplifier

The output from the bolometer supplies the input to a pair of beam-deflection type amplifiers. Each amplifier, with one output vented to ambient and arranged in parallel with another amplifier, supplies an input to the succeeding stage. In this manner, the signal is amplified through the first four stages; however, the output of the fourth stage connects and drives the large, last stage power amplifier as shown. The output of this last stage drives the thrusters (solar vane simulators) and the reaction wheel. The pressure gain of this amplifier package, at normal load, is approximately 77:

$$\text{Pressure Gain} = \frac{\Delta P \text{ out}}{\Delta P \text{ in}} \quad . \qquad (10)$$

The design of the reaction wheel was based on two particular parameters: the time constant (τ) and the inertia (J). The wheel consists of a conical gas bearing attached to the shaft, a rotating cylinder, and the turbine collar. The photograph shows the reaction wheel in Figure 14 and a schematic of the cross-section is presented in Figure 18. Gas (nitrogen) enters the plenum at around 20 psi (137 kN/m^2). The gas bearing was fabricated from a porous graphite material of very low porosity. This particular material was found to

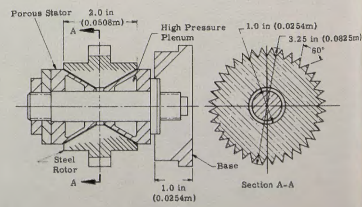

Fig 18. Reaction Wheel

be quite adequate. The flywheel time constant and gain were determined by recording the angular velocity, ω, versus time. A flywheel gain of 26.2 rad/s-psi (3.82 rad/s/kN/m^2) and a time constant of approximately 100 seconds were measured.

To simulate solar pressure on the demonstrator, a technique using small low-gain thrusters was chosen. This choice permitted a large variation in the long-term response mode. By increasing the gain of the thruster, the simulator can return to null in a shorter time interval. The disadvantage of fast return, however, is that the long-term mode control (thrusters) and the short-term mode control (reaction wheel) systems would be insufficiently decoupled and, will therefore interact, necessitating a reanalysis of the system. The gain should be adjusted to desaturate the reaction wheel over a period of about 30 minutes after a 5-degree excursion of the vehicle. A latent advantage of the thrusters is realized when the simulator is initially trimmed. Bias torques (on the simulator) can also be neutralized by adjusting the quiescent power levels of the thrusters.

To simulate the effect of meteor impact on the spacecraft, a metal sphere was impacted on the side of the simulator. A mechanical pendulum arrangement was used quite effectively.

To achieve representative solar radiation, a large (1 kW) photo floodlamp was selected as the source. The light intensity could be varied from a strength of 1 to 10 solar constants (1 solar constant = 0.34 kcal/m^2-s) using a focusing lens system. The lamp was adjusted to yield representative radiation by calibrating the unit for a strength of 1 solar constant at a 6-foot (1.95m) distance. All the included data were taken at this range and at a strength of 1 solar constant.

An operational test was performed on the fluidic components after integration to measure the system's forward loop static gain. Results of this test are presented in Figure 19. The bolometer was given offsets to ±5 degrees in increments of 1 degree and the flywheel's angular velocity measured. The average forward loop gain is 1400 s^{-1}. This curve was reproduced within 5 percent accuracy with no hysteresis determined.

The product of individual component gains should equal the integrated gain.

$$K_f = K_B K_W K_A \qquad (11)$$

where K_B is bolometer gain; K_W, flywheel gain; and K_A, amplifier gain. Applying into the above equation the component gains found previously,

K_B = 0.54 psi/rad (3.7 kN/m^2 rad)

K_W = 26.2 rad/s/psi (3.82 rad/s-kN/m^2)

K_A = 77 psi/psi (77 kN/m^2/kN/m^2)

the forward loop gain can be calculated:

$$K_f = (3.7)(3.82)(77) = 1100\ s^{-1} \qquad (12)$$

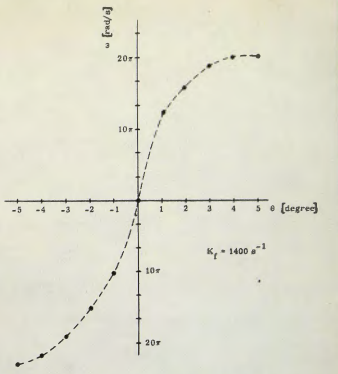

Fig 19. Fluidic System Forward Loop Gain

which agrees with the measured average forward loop gain of 1400 s^{-1} (Figure 19).

Performance

Before any data were taken, the simulator had to be activated and permitted to reach thermal equilibrium (assumed after approximately 2 hours of operation). This length of time seemed necessary to ensure that the thermal transients possibly affecting the control system and main air support bearing assembly had been eliminated and that steady-state thermal conditions existed. Because nitrogen (N_2) at 151 psi (1030 kN/m^2) was supplied to the underside of the air pad to transfer 30 psi (206 kN/m^2) into the control system plenum, considerable expansion and cooling were present. Simultaneously, the floodlight contributed a heating-up effect. Thus this lengthy period was necessary to ensure equilibrium and minimize extraneous thermal effects. After equilibrium was attained, the simulator was uncaged, i.e., the channel beam and reaction wheel were released and allowed to rotate. The system was then trimmed for dynamic equilibrium, i.e., the system maintained a desired heading for approximately 15 minutes.

After dynamic equilibrium was attained, various impacts from the meteor simulator were imposed on the spacecraft simulator and data recorded. In this manner, many curves were generated and their results evaluated. The curves presented in Figure 20, 21, and 22 were selected as representative of most of the data recorded. Figure 20 shows the response of the control system to an initial impact velocity of V_o = 0.133 deg/s. The velocity disturbances are 0.1089 deg/s and 0.083 deg/s in Figures 21 and 22, respec-

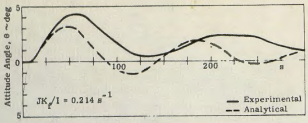

Fig 20. Simulator Response to Impact Velocity of 0.133 deg/s

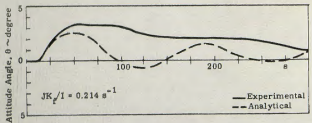

Fig 21. Simulator Response to Impact Velocity of 0.1089 deg/s

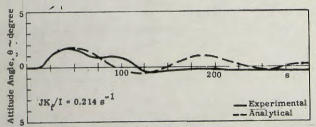

Fig 22. Simulator Response to Impact Velocity of 0.083 deg/s

tively. Based on these disturbances and a normalized gain constant of $0.214\ s^{-1}$, analytical curves were generated and are presented for comparison. All the figures show the capability of the control system to stabilize within 5 degrees and return the space simulator to within ±1 degree.

Despite the lack of close agreement between the predictions and experiment regarding system frequency and damping, the maximum overshoot and steady-state values are considered sufficient to demonstrate the feasibility of a fluidic control system. The amplitude difference between the analytical and experimental curves results principally from the effects of random turbine torques, viscous drag of the simulator motion, and air currents within the laboratory. The size of these disturbance torques that act on the simulator are comparable in magnitude to the fluidic control system's restoring torques. Turbine torques arising from the flow of high velocity gas in the clearance section of the main air bearing and also from the flow issuing from the three trim pads are considered the dominate disturbance torques.

Good correlation of steady-state offsets was obtained since each of the curves converge to within the allowable ±1 degree error within 300 seconds.

The curves shown in Figure 20 compare favorably in frequency. The first node occurs within 10 seconds on the two curves. The frequency of the experimental traces in Figures 21 and 22, however, are not as well defined. In these curves, the response appears considerably damped, with perhaps a slight ring imposed on the waveform.

In summary, these curves present data taken on a spacecraft simulator which had very large disturbance torques. To correct this anomaly would require either an improved air bearing or scaling the simulator to where the attitude control torques are at least a magnitude greater than the disturbance torques.

Conclusions

A single axis fluidic attitude control system has been investigated and a simulator designed and fabricated for the solar probe. Feasibility of applying fluidics for attitude control has been demonstrated; however, many refinements and improvements are required before a final design can be considered[3]. The design and development of a system power supply are necessary. It is expected that the information herein is sufficient to initially design an overall power supply, at least for demonstration purposes.

References

1. Final Report, Martin Marietta Report ER 13110, "Solar Probe Study," (Vol. I-VII), Baltimore, Maryland, 1963

2. de Moraes, C. A., and Gage, D. D., "Mission Objectives and Design Considerations for a Scientific Solar Probe," AIAA Unmanned Spacecraft Meeting, Los Angeles, California, p 413, 1-4 March 1965

3. Final Report, Martin Marietta OR 9004, "Fluidic Attitude Control System - Solar Probe," Orlando, Florida, 1967